Probability distribution and statistical properties of spherically compensated cosmic regions in ΛCDM cosmology

Jean-Michel Alimi, Paul de Fromont

Monthly Notices
of the
ROYAL ASTRONOMICAL SOCIETY

MNRAS **475,** 1912–1924 (2018)
Advance Access publication 2017 November 15

doi:10.1093/mnras/stx2948

Probability distribution and statistical properties of spherically compensated cosmic regions in ΛCDM cosmology

Jean-Michel Alimi★ and Paul de Fromont

LUTH, Observatoire de Paris, PSL Research University, CNRS, Université Paris Diderot, Sorbonne Paris Cité 5 place Jules Janssen, F-92195 Meudon, France

Accepted 2017 November 13. Received 2017 October 11; in original form 2017 September 6

ABSTRACT

The statistical properties of cosmic structures are well known to be strong probes for cosmology. In particular, several studies tried to use the cosmic void counting number to obtain tight constrains on dark energy. In this paper, we model the statistical properties of these regions using the CoSphere formalism (de Fromont & Alimi) in both primordial and non-linearly evolved Universe in the standard Λ cold dark matter model. This formalism applies similarly for minima (voids) and maxima (such as DM haloes), which are here considered symmetrically. We first derive the full joint Gaussian distribution of CoSphere's parameters in the Gaussian random field. We recover the results of Bardeen et al. only in the limit where the compensation radius becomes very large, i.e. when the central extremum decouples from its cosmic environment. We compute the probability distribution of the compensation size in this primordial field. We show that this distribution is redshift independent and can be used to model cosmic voids size distribution. We also derive the statistical distribution of the peak parameters introduced by Bardeen et al. and discuss their correlation with the cosmic environment. We show that small central extrema with low density are associated with narrow compensation regions with deep compensation density, while higher central extrema are preferentially located in larger but smoother over/under massive regions.

Key words: early Universe – large-scale structure of Universe – cosmology: theory.

1 INTRODUCTION

Statistical properties of high-density regions [as dark matter (DM) haloes] or under dense regions (as cosmic voids) have been extensively used to address the main questions of modern cosmology such as the origin of dark energy (DE) or the nature of gravity. Numerous successes have been obtained from the mass function of DM haloes through the Press Schechter formalism (Press & Schechter 1974) or its powerful extensions like Excursion Set Theory (Bond et al. 1991). Predictions using these formalism are generally in very good agreement with numerical simulation results (Sheth & Tormen 1999; Jenkins et al. 2001; Tramonte et al. 2017), but these formalisms do not probe the large-scale environment of DM haloes. Moreover, a full understanding of such cosmological probes needs a full or at least a better understanding of the non-linear evolution of gravitational collapse.

Concerning under dense regions as cosmic voids, it is even more challenging to describe precisely the statistics of such regions (Sheth & van de Weygaert 2004; Achitouv, Neyrinck & Paranjape 2015), mainly because we do not have an objective definition and a physically motivated dynamical model for voids. Both dynamical and statistical properties of cosmic voids depend on their algorithmic definition (Platen, Weygaert & Jones 2007; Neyrinck 2008; Cautun, Cai & Frenk 2016), a full comparative analysis of algorithms for detecting voids in numerical simulations is for example necessary.

In de Fromont & Alimi (2018), labelled thereafter Paper I, we introduced the spherically compensated cosmic regions, named thereafter CoSpheres. Such regions describe the large-scale cosmic environment around local extremum in the density field. CoSphere can be splitted in two distinct radial regions. An over (respectively, under) massive spherical core around the central maximum (respectively, minimum) and an exterior under (respectively, over) massive surrounding belt. By over massive, we mean that the total mass $m(r)$ is higher than the homogeneous mass $4\pi/3\bar{\rho}_m r^3$. In the Newtonian limit, over massive regions collapse (i.e. $\ddot{r} < 0$), while under massive region expand towards larger radii. For each central extremum, the radius separating these two distinct regions is called the compensation radius R_1. By definition, it satisfies $m(R_1) = 4\pi/3\bar{\rho}_m R_1^3$. The origin of CoSpheres within the primordial Gaussian random field (GRF) has been precisely described using the constrained GRF formalism with an appropriate compensation constraint (Paper I). In this primordial Gaussian field, the expected spherically average profiles can be fully parametrized by four independent scalars. Beside the compensation radius R_1, they

★ E-mail: paul.de-fromont@obspm.fr

are described by three *shape* parameters: ν, x, and ν_1. The first parameters x and ν, already introduced by (Bardeen et al. 1986, named thereafter BBKS), qualify the central extrema, while ν_1 defines the compensation density contrast $\delta_1 = \nu_1\sigma_0$ as $\delta(R_1) = \delta_1$.

The non-linear dynamical evolution of CoSpheres is described with high precision through the spherical collapse model. These cosmic regions can be detected in numerical simulations, in Paper I we showed that they can be fully reconstructed from high redshift (within the GRF) until $z = 0$ in Λ cold dark matter (ΛCDM) cosmology. Consequently, these regions can be used as powerful probes for cosmology and gravity itself as it will be investigated in Alimi & de Fromont (in preparation) and de Fromont & Alimi (in preparation) .

While Paper I focused on the construction of these cosmic regions and the derivation of their average density and mass profiles at any redshift, this paper is fully dedicated to the study of their statistical properties. We thus derive the full joint Gaussian probability distribution for the profile parameters R_1, ν, x, and ν_1 in GRF. This distribution measures the probability to obtain a CoSphere with the corresponding parameters in the primordial Gaussian Universe.

We then deduce the one-dimensional probability distribution $\mathrm{d}P(R_1)$ marginalized over the shape parameters ν, x, and ν_1. This distribution is proportional to the count number of compensation radii. It gives the probability to find a R_1 around any extremum. Despite being derived in the primordial Gaussian field, since compensation radii evolve comovingly (Paper I), this distribution is expected to be redshift-independent. Using numerical simulations, we show that it is indeed well conserved during evolution. Interestingly, this size distribution provides a well-defined analytical prediction for cosmic voids sizes once considered as compensated regions around minimum whose size is defined as R_1.

From the full joint Gaussian probability distribution, we also compute the marginalized conditional distribution of the three shape parameters at a given compensation radius R_1. We then derive their constrained moments $\langle \alpha^n | R_1 \rangle$ with $\alpha = \{\nu, x, \nu_1\}$. For $n = 1$, the mean values $\langle \nu | R_1 \rangle$, $\langle x | R_1 \rangle$, and $\langle \nu_1 | R_1 \rangle$ can be used to define the mean average profile at fixed compensation radius. These profiles are expected to reproduce the full matter field of CoSpheres once averaged over all possible stochastic realization, i.e. all possible value for each shape parameters ν, x, and ν_1 given R_1. We then study the shape of the mean average profiles according to R_1 and show that the central extrema progressively tends to the universal BBKS peak profile for large R_1. For small R_1 however, the central extremum is strongly correlated to its cosmic environment through ν_1 and R_1.

Using the spherical collapse model, we derive the exact non-linear evolution of the compensation density distribution $\mathrm{d}P(\delta_1, R_1)$ for any redshift. We compute analytically the evolved moments $\langle \delta_1^n | R_1 \rangle$ for both cosmic voids (central minimum) and central over densities. We compare our results with numerical simulation and show that the agreement is very good, even in the non-linear regime.

This paper is organized as follows: in the first section, we define precisely CoSpheres and their compensation radius R_1. We also discuss how such cosmic regions are detected in numerical simulation. In Section 3, we derive the statistical properties of these regions in the primordial Gaussian field, the radii distribution $\mathrm{d}P(R_1)$ together with the statistical study of the shape parameters. We discuss the properties of the mean averaged density profile at fixed compensation radius R_1. In the last section, Section 4, we study the dynamical properties of these distribution by using the Lagrangian spherical collapse and compare the results to numerical simulations at $z = 0$ in ΛCDM cosmology.

2 COSPHERES IN THE SKY

We study the statistical properties of CoSpheres. These cosmic structures are defined around extrema (minima or maxima) in the density field at any redshift (Paper I). Around each extremum, we define the concentric mass $m(r)$ as the mass enclosed in the sphere of radius r, from which we deduce the spherical mass contrast $\Delta(r)$ as

$$\Delta(r) := \frac{m(r)}{4\pi/3\bar{\rho}_\mathrm{m} r^3} - 1 \tag{1}$$

This profile is linked to the density contrast $\delta(r) = \rho_\mathrm{m}(r)/\bar{\rho}_\mathrm{m} - 1$ through

$$\Delta'(r) = \frac{3}{r}\left[\delta(r) - \Delta(r)\right] \Leftrightarrow \Delta(r) = \frac{3}{r^3}\int_0^r u^2\delta(u)\mathrm{d}u \tag{2}$$

where $\Delta'(r) = \partial\Delta(r)/\partial r$. As discussed in Paper I, each extremum must be compensated on a finite scale. For each spherical profile, it exists a unique scale R_1 called *compensation radius* satisfying.

$$\Delta(R_1) = 0 \tag{3}$$

R_1 is defined as the smallest radius satisfying equation (3). This scale measures the size of the over (respectively, under) massive region[1] surrounding each maximum (respectively, minimum). Since $\ddot{r} \propto -\Delta(r)$ in Newtonian regime, the mass contrast $\Delta(r)$ drives the local gravitational collapse. The compensation radius separates the collapsing and the expanding regions.

These regions can be detected in numerical simulations. We use in this work, the numerical simulations from the 'Dark Energy Universe Simulation' project, publicly available through the 'Dark Energy Universe Virtual Observatory' Database.[2] These simulations consist of N-body simulations of DM for realistic DE models. For more details, we refer the interested reader to dedicated sections in Alimi et al. (2010), Alimi et al. (2012), Rasera et al. (2010), Courtin et al. (2011), and Reverdy et al. (2015). We focus in this paper on the flat ΛCDM model with parameters calibrated against measurements of *WMAP* 5-yr data (Komatsu et al. 2009) and luminosity distances to supernova Type Ia from the UNION data set (Kowalski et al. 2008).

The reduced Hubble constant is set to $h = 0.72$ and the cosmological parameters are $\Omega_\mathrm{DE} = 0.74$, $\Omega_\mathrm{b} = 0.044$, $n_\mathrm{s} = 0.963$, and $\sigma_8 = 0.79$. All along this work, The *reference simulation* is chosen with $L_\mathrm{box} = 2592\,h^{-1}\mathrm{Mpc}$ and $n_\mathrm{part} = 2048^3$. It provides both a large volume and a good mass resolution. Here, the mass of one particle is $m_\mathrm{p} \sim 1.5 \times 10^{11}\,h^{-1}\,\mathrm{M}_\odot$.

The construction procedure of numerical CoSpheres consists first in finding the position of local extremum. In the case of a central overdensity, we identify maxima with the centre of mass of DM haloes. Haloes are founded by a friend-of-friend algorithm with a linking length $b = 0.2$. We considered in the reference simulation 200000 haloes with a mass $M_\mathrm{h} \sim 3 \times 10^{13}\,h^{-1}\,\mathrm{M}_\odot$. Selecting haloes with a mass M_h is equivalent to impose a threshold on the height of their progenitor, i.e. it selects local extrema with $\nu \geq \nu_0 = \delta_\mathrm{c}/\sigma_0(M_\mathrm{h})$, where $\delta_\mathrm{c} \simeq 1.686$ for ΛCDM cosmology and $\sigma_0(M_\mathrm{h})$ is the fluctuation level.

For central underdensities, we smooth the density field with a Gaussian kernel on a few number of cells. Minima are founded by comparing the local density of each cell to its neighbours. The centre of the cell is then identified with the position of the local

[1] Not to be confused with over/underdense regions.
[2] http://www.deus-consortium.org/deus-data/

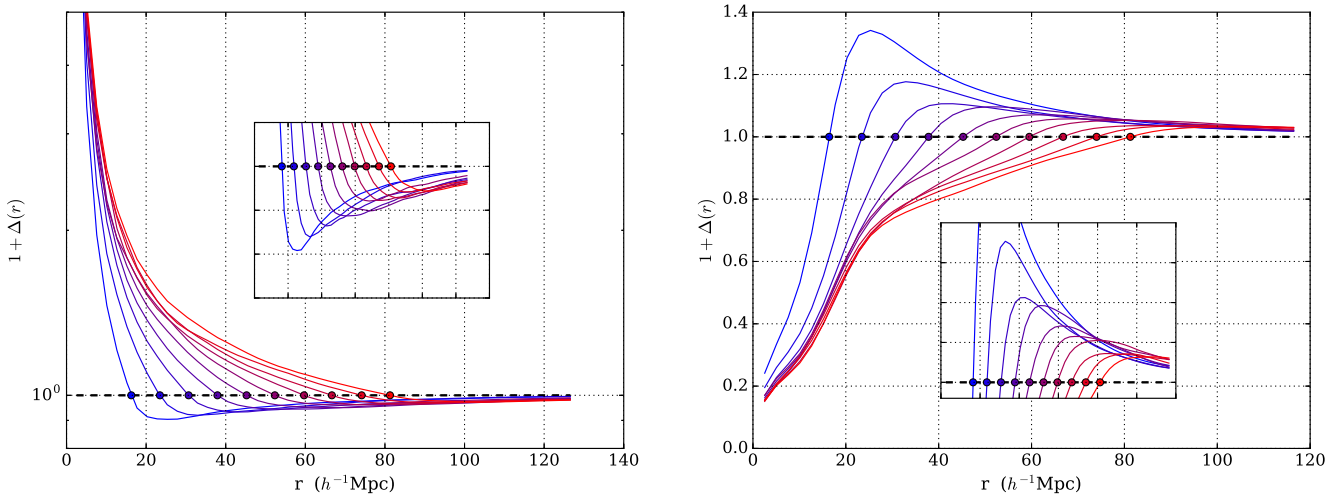

Figure 1. Radial average mass contrast at $z = 0$ in the reference simulation. Each colour corresponds to a given compensation radius R_1 from 15 to 80 h^{-1}Mpc . Whereas each single individual profile is far from a smooth curve, stacked profiles display a global shape with well-defined properties. The inset plots zoom on the compensation region, i.e. the under (respectively, over) massive regions for central maximum (respectively, minimum).

minimum. The backward procedure is simplistic and assumes that the comoving position of each void is conserved during cosmic evolution. At any redshift, each void's position is assumed to be the same than the one detected at $z = 0$.

From each extrema, we compute the concentric mass $m(r)$ from DM particles

$$m(r) = \sum_i m_{\rm p} \Theta \left[r - |\boldsymbol{x}_{\rm i} - \boldsymbol{x}_0| \right] \tag{4}$$

where $m_{\rm p}$ is the mass of one particle, $\boldsymbol{x}_{\rm i}$ the position of the ith particle, and $\boldsymbol{x}_0$ the position of the central extremum. $\Theta(x)$ is the standard Heaviside distribution such as $\Theta(x) = 1$ if $x > 0$ and 0 elsewhere.

The second step consists into building average profiles by stacking together individual profiles with the same compensation radius. For each R_1, we take at least 1000 profiles for both haloes and voids in order to ensure a fair statistics. In Fig. 1, we show the resulting average profiles for both central over and under densities and several compensation radii at $z = 0$ in the reference simulation. As claimed before, the radial structure of these regions is symmetric; a central over (respectively, under) massive core until $r = R_1$ surrounded by a large under (respectively, over) massive compensation belt for $r \geq R_1$.

Numerical simulations can be used to follow the gravitational evolution of CoSpheres. By definition, these regions are detected at $z = 0$. For a central maximum, i.e. build from DM halo, we identify the position of its progenitor at higher redshift to the centre of mass of its particles at $z = 0$. For each halo detected today, this procedure provides an estimated position of its progenitor at other redshift. These positions are used to define CoSpheres for any $z \neq 0$.

3 STATISTICS OF COSPHERES IN GAUSSIAN RANDOM FIELDS

In this section, we study the statistical properties of CoSpheres in the framework of GRF with appropriate constraints (Paper I).

3.1 Gaussian random fields, the basics

Let us first recall the basic elements necessary for the derivation of average quantities in GRF. We consider here an homogeneous, isotropic random field whose statistical properties are fully determined by its power spectrum (or spectral density) $P(k)$. It can be written as the Fourier transform of the auto-correlation of the field $\xi(r) = \xi(|\boldsymbol{x}_1 - \boldsymbol{x}_2|) = \langle \delta(\boldsymbol{x}_1)\delta(\boldsymbol{x}_2) \rangle$:

$$\xi(r) = \frac{1}{2\pi^2} \int_0^{+\infty} k^2 P(k) \frac{\sin(kr)}{kr} {\rm d}k \tag{5}$$

The Gaussianity of the field $\delta(\boldsymbol{x})$ leads to the joint probability

$${\rm d}\mathcal{P}_{\rm N} = P\left[\delta(\boldsymbol{x}_1), ..., \delta(\boldsymbol{x}_{\rm N})\right] {\rm d}\delta(\boldsymbol{x}_1)...{\rm d}\delta(\boldsymbol{x}_{\rm N}) \tag{6}$$

that the field has values in the range $[\delta(\boldsymbol{x}_{\rm i}), \delta(\boldsymbol{x}_{\rm i}) + {\rm d}\delta(\boldsymbol{x}_{\rm i})]$ for each position $\boldsymbol{x}_{\rm i}$. In this GRF model, it is

$${\rm d}\mathcal{P}_{\rm N} = \frac{1}{\sqrt{(2\pi)^N \det \boldsymbol{M}}} \exp\left[-\frac{1}{2} \boldsymbol{\delta}^t \cdot \boldsymbol{M}^{-1} \cdot \boldsymbol{\delta} \right] \prod_{i=1}^{N} {\rm d}\delta_{\rm i} \tag{7}$$

$\boldsymbol{\delta}$ is the N-dimensional vector $\delta_{\rm i} = \delta(\boldsymbol{x}_{\rm i})$ and $\boldsymbol{M}$ is the $N \times N$ covariance matrix, here fully determined by the field auto-correlation

$$M_{\rm ij} := \left\langle \delta_{\rm i} \delta_{\rm j} \right\rangle = \xi(|\boldsymbol{x}_{\rm i} - \boldsymbol{x}_{\rm j}|) \tag{8}$$

where the average operator $\langle ... \rangle$ denotes thereafter an ensemble average on every statistical configuration of the field. Using the ergodic theorem, this mean can be identified with the spatial average of the same quantity. The average of any operator X can be computed from the mean of its Fourier component $\tilde{X}(k)$

$$\langle X \rangle := \frac{1}{2\pi^2 \sigma_0^2} \int_0^{+\infty} k^2 P(k) \tilde{X}(k) {\rm d}k = \frac{\int_0^{+\infty} k^2 P(k) \tilde{X}(k) {\rm d}k}{\int_0^{+\infty} k^2 P(k) {\rm d}k} \tag{9}$$

where the fluctuation rms is

$$\sigma_0 = \left[\frac{1}{2\pi^2} \int_0^{+\infty} k^2 P(k) {\rm d}k \right]^{1/2} \tag{10}$$

Furthermore, we are interested in deriving the properties of the field subject to a set of linear constraints $\boldsymbol{C} = \{C_1, ..., C_{\rm n}\}$. Following

Bertschinger (1987), each constraint C_i can be written as

$$C_\mathrm{i}[\delta] := \int W_\mathrm{i}(\boldsymbol{x}_\mathrm{i} - \boldsymbol{x})\delta(\boldsymbol{x})\mathrm{d}\boldsymbol{x} = c_\mathrm{i} \tag{11}$$

where W_i is the corresponding window function and c_i its value. For example, constraining the value of the field to a certain δ_0 at some point $\boldsymbol{x}_0$ leads to $W_\mathrm{i} = \delta_\mathrm{D}(\boldsymbol{x} - \boldsymbol{x}_0)$ and $c_\mathrm{i} = \delta_0\mathrm{m}$ where δ_D is the Dirac delta. For n constraints, the joint probability $\mathrm{d}\mathcal{P}[\boldsymbol{C}]$ that the field satisfies these conditions reaches (van de Weygaert & Bertschinger 1996; Bertschinger 1987)

$$\mathrm{d}\mathcal{P}[\boldsymbol{C}] = \frac{1}{\sqrt{(2\pi)^n \det \boldsymbol{Q}}} \exp\left[-\frac{1}{2}\boldsymbol{C}^t \cdot \boldsymbol{Q}^{-1} \cdot \boldsymbol{C}\right] \prod_{i=1}^{n} \mathrm{d}c_\mathrm{i} \tag{12}$$

where $\boldsymbol{Q}$ is the covariance matrix of the constraints defined through $\boldsymbol{Q} = \langle \boldsymbol{C}^t \cdot \boldsymbol{C} \rangle$.

3.2 The full joint Gaussian probability distribution

In this section, we derive the full joint Gaussian probability to find a CoSphere with a given set of parameters in GRF. Since these regions are build around extremum, we must include the peak conditions derived by BBKS. A local extrema located at $\boldsymbol{x}_0$ is defined by three conditions

$$\delta(\boldsymbol{x}_0) = \nu\sigma_0 \tag{13}$$

$$\eta_\mathrm{i} = \frac{\partial\delta(\boldsymbol{x}_0)}{\partial x_\mathrm{i}} = 0 \tag{14}$$

$$\zeta_\mathrm{ij} = \frac{\partial^2\delta(\boldsymbol{x}_0)}{\partial x_\mathrm{i}\partial x_\mathrm{j}} \tag{15}$$

where equation (13) gives the height of the peak in unit of the fluctuation level (see equation 10), whereas equation (14) imposes that the local gradient $\boldsymbol{\eta}$ vanishes (since we consider extrema). Equation (15) defines the Hessian matrix $\boldsymbol{\zeta}$ of the density profile around the peak.

In addition to the peak condition, we must explicitly encode the compensation condition equation (3). This is achieved by adding the new constraints (Paper I)

$$C_{R_1}[\delta] := \int \Theta\left(R_1 - |\boldsymbol{x} - \boldsymbol{x}_0|\right)\delta(\boldsymbol{x})\mathrm{d}\boldsymbol{x} = \bar{\nu}\sigma_0 = 0 \tag{16}$$

$$C_{\nu_1}[\delta] := \int \delta_D\left(R_1 - |\boldsymbol{x} - \boldsymbol{x}_0|\right)\delta(\boldsymbol{x})\mathrm{d}\boldsymbol{x} = \nu_1\sigma_0 \tag{17}$$

where Θ is the Heaviside step function and δ_D is the usual Dirac delta. Equation (16) is the transposition of equation (3) in the form equation (11). The parameter $\bar{\nu}$ is defined by $\Delta(R_1) = \bar{\nu}\sigma_0$ and is set to 0 by definition of the compensation radius R_1. Equation (17) defines the compensation density on the sphere of radius R_1 such that $\delta(R_1) := \delta_1 = \nu_1\sigma_0$.

3.2.1 The full joint probability for spherically compensated peaks

Without any assumption on the symmetry, CoSpheres in primordial field are described by 12 independent scalars $(\nu, \bar{\nu}, \nu_1, \eta_1, \eta_2, \eta_3, \text{and}\zeta_\mathrm{ij})$ with i and j running in $\{1, 2, 3\}$. The computation of the conditional probability equation (12) involves the correlation matrix $\boldsymbol{Q}$ between these 12 constraints. The introduction of two new degree of freedom makes the computation of $\boldsymbol{Q}$ more complicated than for a standard unconstrained peak. However, following BBKS, we can simplify $\boldsymbol{Q}$ by introducing the reduced variables linked to the local curvature of the profile around the peak

$$x = -\frac{\zeta_{11} + \zeta_{22} + \zeta_{33}}{\sigma_0\sqrt{\langle k^4\rangle}}, \quad y = -\frac{\zeta_{11} - \zeta_{33}}{2\sigma_0\sqrt{\langle k^4\rangle}},$$
$$z = -\frac{\zeta_{11} - 2\zeta_{22} + \zeta_{33}}{2\sigma_0\sqrt{\langle k^4\rangle}}$$

where the various moments of $P(k)$ are given by

$$\langle k^{2n}\rangle := \frac{\sigma_n^2}{\sigma_0^2} = \frac{1}{2\pi^2\sigma_0^2}\int_0^{+\infty} k^{2+2n}P(k)\mathrm{d}k \tag{18}$$

y and z quantify the asymmetry of the profile around the peak, whereas x defines the local curvature. It is directly related to the spherical density profile by

$$\lim_{r\to 0}\frac{\partial^2\delta(r)}{\partial r^2} = -\frac{x}{3}\sigma_0\sqrt{\langle k^4\rangle} \tag{19}$$

With these variables, $\boldsymbol{Q}$ reduces to a partitioned matrix where the only non-diagonal terms are included in a 4×4 sub-matrix $\tilde{\boldsymbol{Q}}$. This sub-matrix encodes the new correlations introduced by R_1 (or $\bar{\nu}$ equivalently) and ν_1. In the $(\nu, \bar{\nu}, x, \nu_1)$ basis, it reaches

$$\tilde{\boldsymbol{Q}} = \begin{pmatrix} 1 & \langle W_1\rangle & \frac{\langle k^2\rangle}{\sqrt{\langle k^4\rangle}} & \langle J_1\rangle \\ \langle W_1\rangle & \langle W_1^2\rangle & \frac{\langle k^2 W_1\rangle}{\sqrt{\langle k^4\rangle}} & \langle W_1 J_1\rangle \\ \frac{\langle k^2\rangle}{\sqrt{\langle k^4\rangle}} & \frac{\langle k^2 W_1\rangle}{\sqrt{\langle k^4\rangle}} & 1 & \frac{\langle k^2 J_1\rangle}{\sqrt{\langle k^4\rangle}} \\ \langle J_1\rangle & \langle W_1 J_1\rangle & \frac{\langle k^2 J_1\rangle}{\sqrt{\langle k^4\rangle}} & \langle J_1^2\rangle \end{pmatrix} \tag{20}$$

where we used the following notation for the spherical Bessel functions evaluated at R_1.

$$W_1 := 3\frac{\sin(kR_1) - kR_1\cos(kR_1)}{(kR_1)^3} \tag{21}$$

$$J_1 := \frac{\sin(kR_1)}{kR_1} \tag{22}$$

We can now rewrite equation (12) as

$$\mathrm{d}^{12}\mathcal{P}(\nu, \bar{\nu}, x, \nu_1, y, z, \boldsymbol{\eta}, \zeta_4, \zeta_5, \zeta_6) \propto \frac{1}{\sqrt{\det \boldsymbol{Q}}}\exp\left[-\frac{1}{2}\mathcal{F}\right]\mathcal{D} \tag{23}$$

where the superscript 12 indicates that this is 12-dimensional quantity with the measure $\mathcal{D} = \mathrm{d}\nu\mathrm{d}\bar{\nu}\mathrm{d}x\mathrm{d}\nu_1\mathrm{d}y\mathrm{d}z\prod_{i=4}^{6}\mathrm{d}\zeta_\mathrm{i}\prod_l \mathrm{d}\eta_\mathrm{l}$ with $\zeta_4 = \zeta_{23}$, $\zeta_5 = \zeta_{13}$, and $\zeta_6 = \zeta_{12}$ BBKS.

We now neglect the numerical factors which do not depend explicitly on R_1. The two form $\mathcal{F}$ reduces to

$$\mathcal{F} = \frac{x^2 C_\mathrm{x} + \nu^2 C_\nu + \nu_1^2 C_{\nu_1} + 2\left(x\nu C_{\mathrm{x}\nu} + x\nu_1 C_{\mathrm{x}\nu_1} + \nu_1\nu C_{\nu_1\nu}\right)}{\Sigma^2(R_1)} + 15y^2 + 5z^2 \tag{24}$$

where we have already imposed the condition $\eta_\mathrm{i} = 0$ (see equation 14) and $\bar{\nu} = 0$ (see equation 16). The C_α functions (with $\alpha = 0$, x, ν, ν_1, $x\nu$, $x\nu_1$, $\nu_1\nu$) depend also on R_1. Their explicit form is given in Appendix A. $\Sigma^2(R_1)$ takes the form

$$\Sigma^2(R_1) = C_0 + C_\mathrm{x} + C_\nu + 2\frac{\langle k^2\rangle}{\sqrt{\langle k^4\rangle}}C_{\mathrm{x}\nu} \tag{25}$$

Since we consider only spherical profiles, we marginalize over the asymmetry parameters y and z. The integration of $\mathrm{d}\mathcal{P}$ over y and z, combined with the ordering condition $|\zeta_{11}| \geq |\zeta_{22}| \geq |\zeta_{33}| \geq 0$ then leads to the four-dimensional joint probability for the spherically compensated cosmic regions

$$\mathrm{d}^4\mathcal{P}(\nu, x, \bar{\nu}, \nu_1) \propto \frac{f(x)}{\Sigma(R_1)} \exp\left[-\frac{\mathcal{L}(x, \nu, \nu_1)}{2}\right] \mathrm{d}\nu \mathrm{d}x \mathrm{d}\bar{\nu} \mathrm{d}\nu_1 \tag{26}$$

with BBKS

$$f(x) = \sqrt{\frac{2}{5\pi}}\left[e^{-\frac{5x^2}{2}}\left(-\frac{8}{5}+\frac{x^2}{2}\right)+e^{-\frac{5x^2}{8}}\left(\frac{8}{5}+\frac{31x^2}{4}\right)\right] + \frac{x^3-3x}{2}\left[\mathrm{Erf}\left(x\sqrt{\frac{5}{8}}\right)+\mathrm{Erf}\left(x\sqrt{\frac{5}{2}}\right)\right]$$

This function is not modified here because it results from the integration over the y and z variables which are not correlated to ν_1 nor $\bar{\nu}$. We define $\mathcal{L}$ as $\mathcal{L} := \mathcal{F} - 15y^2 - 5z^2$, i.e.

$$\mathcal{L}(x, \nu, \nu_1, R_1) = \frac{x^2 C_{\mathrm{x}} + \nu^2 C_\nu + \nu_1^2 C_{\nu_1}}{\Sigma^2(R_1)} + 2\frac{x\nu C_{\mathrm{x}\nu} + x\nu_1 C_{\mathrm{x}\nu_1} + \nu_1\nu C_{\nu_1\nu}}{\Sigma^2(R_1)} \tag{27}$$

Note that $\mathcal{L}$ depends on R_1 through Σ and the various C_α functions. When R_1 becomes very large, we recover the BBKS limit (see below Section 3.2.3) and $\mathcal{L}$ reduces to its expression as derived in BBKS. Finally, we map $\bar{\nu}$ to the compensation radius as

$$\mathrm{d}\bar{\nu} = \left|\frac{3\nu_1}{R_1}\right| \mathrm{d}R_1 \tag{28}$$

and we get the full joint Gaussian probability distribution of Co-Spheres

$$\mathrm{d}^4\mathcal{P}(\nu, x, \nu_1, R_1) \propto \frac{|\nu_1|\, f(x)}{R_1 \Sigma(R_1)} \exp\left[-\frac{\mathcal{L}(x, \nu, \nu_1, R_1)}{2}\right] \times \mathrm{d}\nu \mathrm{d}x \mathrm{d}\nu_1 \mathrm{d}R_1 \tag{29}$$

where both $\Sigma(R_1)$ and $\mathcal{L}$ depend on R_1.

3.2.2 *The first crossing condition*

Our definition of R_1 (see equation 3) implicitly assumes that R_1 is the first crossing radius such as $\Delta(R_1) = 0$. However, neither equation (3) nor the definition of ν_1 ensures it. For each R_1, there is a subdomain for the shape parameters where the corresponding average mass contrast profile vanishes at some effective radius $\tilde{R}_1 < R_1$. This is typically the case for central peaks with high curvature x. The true joint Gaussian probability must take this effect into account. In Paper I, we show that the average mass contrast profile corresponding to a set of shape parameters ν, x, and ν_1 can be expressed as

$$\Delta(r) = \sigma_0\left[\nu\Delta_\nu(r) + x\Delta_{\mathrm{x}}(r) + \nu_1\Delta_{\nu_1}(r)\right] \tag{30}$$

where each $\Delta_\alpha(r)$ function involves the compensation scale R_1 and the radius r. This set of shape parameters is safe if it satisfies

$$\forall r \in [0, R_1[, \quad \begin{cases} \Delta(r) > 0 & \text{if} \quad \nu > 0 \\ \Delta(r) < 0 & \text{if} \quad \nu < 0 \end{cases} \tag{31}$$

This defines the safe domain $\mathcal{D}(R_1)$ for $\{\nu, x, \nu_1\}$ where the first radius where $\Delta(r)$ vanishes is R_1. If $\{\nu, x, \nu_1\} \notin \mathcal{D}(R_1)$, there exist an effective $\tilde{R}_1 < R_1$ satisfying

$$\nu\Delta_\nu(\tilde{R}_1) + x\Delta_{\mathrm{x}}(\tilde{R}_1) + \nu_1\Delta_{\nu_1}(\tilde{R}_1) = 0 \tag{32}$$

This effective compensation radius is associated with a compensation density $\tilde{\nu}_1$ defined a

$$\tilde{\nu}_1 = \nu\delta_\nu(\tilde{R}_1) + x\delta_{\mathrm{x}}(\tilde{R}_1) + \nu_1\delta_{\nu_1}(\tilde{R}_1) \tag{33}$$

such that both $\tilde{R}_1$ and $\tilde{\nu}_1$ are functions of ν, x, ν_1, and R_1. The condition equation (31) defining the safe domain $\mathcal{D}(R_1)$ can be translated to a simple restriction on the curvature x

$$|x| < x_{\mathrm{c}}(\nu, \nu_1, R_1) = \min\Big(-|\nu|\frac{\Delta_\nu(r)}{\Delta_{\mathrm{x}}(r)} - |\nu_1|\frac{\Delta_{\nu_1}(r)}{\Delta_{\mathrm{x}}(r)}, \times \forall r < R_1\Big) \tag{34}$$

At fixed R_1, if $|x| \geq x_{\mathrm{c}}(\nu, \nu_1, R_1)$, then this set of parameters $\{R_1, \nu, x, \nu_1\}$ will contribute to $\{\tilde{R}_1, \nu, x, \tilde{\nu}_1\}$, where $\tilde{R}_1$ and $\tilde{\nu}_1$ are the effective parameters defined in equations (32) and (33).

In other words, for each R_1, there is a fraction of its parameter's domain contributing to smaller $R_1^- < R_1$, while a fraction of larger compensation radii with $R_1^+ > R_1$ also contribute to this R_1. The full joint Gaussian probability can thus be formally decomposed in two parts

$$\mathrm{d}^4\mathcal{P}_{\mathrm{tot}}(\nu, x, \nu_1, R_1) \propto \underbrace{\Theta(x_{\mathrm{c}}(\nu, \nu_1, R_1) - |x|)\mathrm{d}^4\mathcal{P}(\nu, x, \nu_1, R_1)}_{\text{direct contribution}} + \underbrace{\int_{R_1}^{\infty}\mathrm{d}R_1^+\int_{-\infty}^{0}\mathrm{d}\nu_1^+\mathrm{d}^4\mathcal{P}(\nu, x, \nu_1^+, R_1^+)\delta_{\mathrm{D}}(\tilde{R}_1 - R_1)\delta_{\mathrm{D}}(\tilde{\nu}_1 - \nu_1)}_{\text{contribution from higher compensation radii}} \tag{35}$$

The first term accounts for peaks satisfying the first crossing condition (FCC), while the second one is the contribution from peaks with higher compensation radii whose effective compensation radius $\tilde{R}_1$ equals R_1 and effective compensation density $\tilde{\nu}_1$ equals ν_1. Note that naturally, this indirect contribution term provides x satisfying equation (34).

3.2.3 *The large-scale limit and the BBKS distribution*

In this section, we focus on the very large-scale behaviour of the full joint Gaussian probability distribution, i.e. when $R_1 \to +\infty$.

For clarity, let us assume a power-law matter power spectrum smoothed with a Gaussian kernel, $P(k) \sim k^n \exp(-k^2 R_{\mathrm{f}}^2)$, where the power index n is the effective power index at very small k and R_{f} the smoothing scale. In the limit $R_1 \to +\infty$, the C_α parameters (see Appendix A) reduce to simple power laws

$$C_{\mathrm{x}} \propto \left(\frac{R_1}{R_{\mathrm{f}}}\right)^{-5-n} \tag{36}$$

$$\frac{C_\nu}{C_{\mathrm{x}}} = 1, \quad \frac{C_{\nu_1}}{C_{\mathrm{x}}} \propto \left(\frac{R_1}{R_{\mathrm{f}}}\right)^2 \tag{37}$$

$$\frac{C_{\mathrm{x}\nu}}{C_{\mathrm{x}}} = -\gamma, \quad \frac{C_{\nu_1\mathrm{x}}}{C_{\mathrm{x}}} \propto \left(\frac{R_1}{R_{\mathrm{f}}}\right)^{-1-n}, \quad \frac{C_{\nu_1\nu}}{C_{\mathrm{x}}} \propto \left(\frac{R_1}{R_{\mathrm{f}}}\right)^{-1-n} \tag{38}$$

$$\frac{C_0}{C_{\mathrm{x}}} \to \gamma^2 - 1 \tag{39}$$

where $\gamma := \langle k^2\rangle / \sqrt{\langle k^4\rangle}$. Using these limits, the exponential term $\mathcal{L}$ simplifies to

$$\mathcal{L}_\infty(x, \nu, \nu_1, R_1) \simeq \frac{x^2 + \nu^2 - 2\gamma x\nu}{1-\gamma^2} + 2\epsilon R_1^2\nu_1^2 + \mathcal{O}\left(R_1^{-1-n}\right) \tag{40}$$

where ϵ is a positive parameter independent from R_1. We note two features for $\mathcal{L}$. The first concerns the (x, ν) dependence which takes the same exact form than in BBKS. The second concerns the term involving ν_1. It depends explicitly on R_1 and contributes to an overall $\exp(-\epsilon\nu_1^2 R_1^2)$ factor in the full joint probability equation (35). For $R_1 \to +\infty$, combined with the $|\nu_1|$ pre-factor appearing in equation (35), it leads to a global $\delta_{\rm D}(\nu_1)$ such that full joint probability distribution reduces to

$$\mathrm{d}\mathcal{P}(\nu, x, \nu_1, R_1)R_1 \to +\infty \to \mathrm{d}\mathcal{P}_{\rm bbks}(x, \nu) \times \frac{\delta_D(\nu_1)}{R_1^{(1-n)/2}}\mathrm{d}\nu_1\mathrm{d}R_1 \quad (41)$$

where $\mathrm{d}\mathcal{P}_{\rm bbks}(\nu, x)$ is the standard joint probability peak derived in BBKS. This limit shows that a central peak with a very large compensation radius is decorrelated from its cosmic environment. As a matter of fact, the full joint probability distribution (see equation 41) is separated in two independent parts, one concerning the local extrema (ν and x only) and the other involving R_1 and ν_1, i.e. concerning its large-scale environment.

The FCC (see Section 3.2.2) condition constraining the value of x (see equation 34) deeply simplifies in this large radii regime where it reduces to

$$|x| \leq \frac{\nu}{\gamma} \quad (42)$$

This means that the statistical properties of the central extrema involving x and ν reduce, for very large compensation radius, to the standard 'unconstrained' peak statistic of BBKS with smaller central curvature satisfying equation (42).

We emphasize that equation (41) illustrates the progressive decoupling between the central peak and its environment. Large R_1 will be associated with universal central peaks whose local shape and properties are similar to BBKS.

3.3 Statistical properties of the shape parameters in GRF

Large-scale density and mass profiles of CoSpheres are described by four parameters within GRF (Paper I). These parameters are

(i) ν and x (defined, respectively, in equations 13 and 19) characterizing the central extremum BBKS,
(ii) the compensation radius R_1 itself (see equation 16) quantifying the size of the over/under massive sphere surrounding the central extremum,
(iii) the reduced compensation density ν_1 (see equation 17) defined on the compensation sphere by $\delta(R_1) \equiv \delta_1 = \nu_1\sigma_0$.

This section is devoted to the study of the statistical properties of these shape parameters. First, we compute the probability distribution of the compensation radius R_1 by marginalizing over the three other shape parameters. It provides the probability to find a R_1 whatever the central extrema and δ_1. We then compute the marginalized conditional probability $\mathrm{d}\mathcal{P}(X|R_1)$ for each shape parameter $X = \{\nu, x, \nu_1\}$ at fixed compensation radius. We use this distribution to deduce their conditional moments $\langle X^n|R_1\rangle$ within GRF. We finally discuss the physical properties of the mean average radial matter profile involving the mean value $\langle X|R_1\rangle$ for each shape parameter X.

In this whole section, we assume central maxima with $\nu > 0$, $x > 0$, and $\nu_1 < 0$. The treatment of the symmetric case (central underdensity) is exactly symmetric and leads to the same results with the following substitutions $x \to -x$, $\nu \to -\nu$, and $\nu_1 \to -\nu_1$ and the appropriate integration domains.

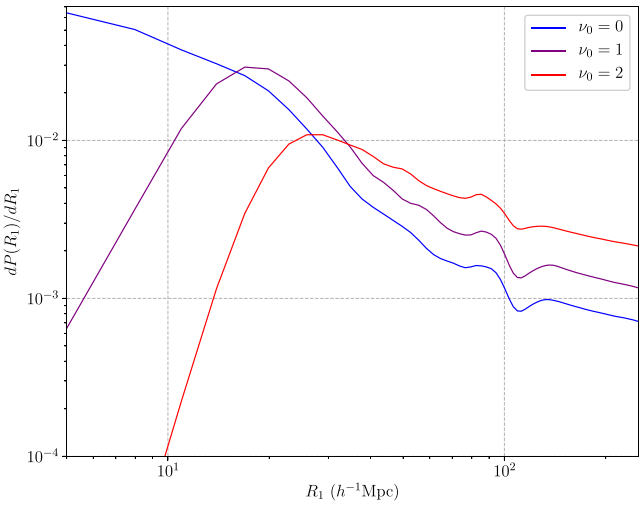

Figure 2. Pdffor the compensation radius in GRF as computed in equation (43). Each curve corresponds to a different threshold ν_0 which defines the minimal height of the central extremum, i.e. $|\nu| \geq |\nu_0|$. Higher thresholds promote larger compensation radii. The most probable R_1 thus increases with ν_0. For this figure, the R_1 pdf is normalized such that $\int_0^{300} \mathrm{d}P(R_1) = 1$ and the power spectrum has been smoothed with a Gaussian kernel on $R_{\rm g} = 5$ h^{-1}Mpc .

3.3.1 *The compensation radius probability distribution*

Each extremum can be associated with a unique R_1 separating the collapsing and the expanding shells. The probability $\mathrm{d}P(R_1)$ to find a local extremum with R_1 and whatever the other shape parameters is obtained by marginalizing equation (35) over the three shape parameters ν, x, and ν_1, leading to

$$\frac{\mathrm{d}P(R_1)}{\mathrm{d}R_1} = \alpha \int_{\nu_0}^{+\infty} \mathcal{J}_{0,0}(\nu, R_1)\mathrm{d}\nu \quad (43)$$

with α a normalization factor, insuring that $\int_0^{+\infty} \mathrm{d}P(R_1) = 1$

$$\alpha^{-1} = \int_0^{+\infty}\int_{\nu_0}^{+\infty} \mathcal{J}_{0,0}(\nu, R_1)\mathrm{d}\nu\mathrm{d}R_1 \quad (44)$$

and the function

$$\mathcal{J}_{0,0}(\nu, R_1) := \int_{-\infty}^{0}\int_0^{x_c} \frac{\mathrm{d}^4\mathcal{P}_{\rm tot}(\nu, x, \nu_1, R_1)}{\mathrm{d}\nu\mathrm{d}R_1} \quad (45)$$

where the integration on the local curvature x is done over $[0, x_{\rm c}(\nu, \nu_1)]$ due to the FCC condition (see Section 3.2.2). Note that the integration over ν_1 goes from $-\infty$ to 0, since we consider here a central maxima.

In Fig. 2, we show this compensation radius probability $\mathrm{d}P(R_1)$ for ΛCDM cosmology in a GRF. We illustrate the effect of the central threshold ν_0 defining the height of the central extrema $|\nu| \geq |\nu_0|$. Increasing the central threshold favours larger compensation radii. This seems natural since higher central peaks are more likely compensated on large regions than smaller ones. This figure also shows typical wiggles in this distribution around $R_1 \sim 100\ h^{-1}$Mpc . This feature is probably related to the BAO. The enhanced correlation on this scale increases the probability to find CoSpheres compensated around this particular radius.

3.3.2 *The compensation density* δ_1

The density contrast $\delta = \nu_1\sigma_0$ is measured on the compensation sphere at $r = R_1$. To get the joint probability for ν_1 and R_1, we

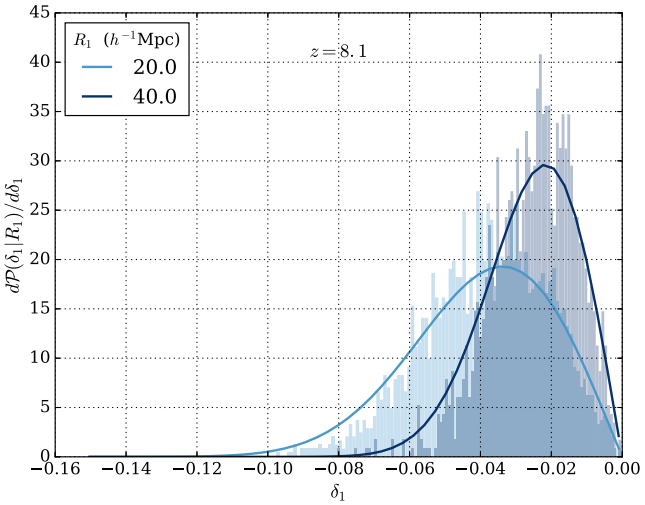

Figure 3. Probability density function $d\mathcal{P}(\delta_1|R_1)/d\delta_1$ computed from equation (47) in the Gaussian field at $z = 8.1$. Curves are the theoretical expectations for the ΛCDM model, while the shaded regions are the measured distributions in the reference simulation for two different compensation radius in the case of a central maximum (thus negative values of δ_1).

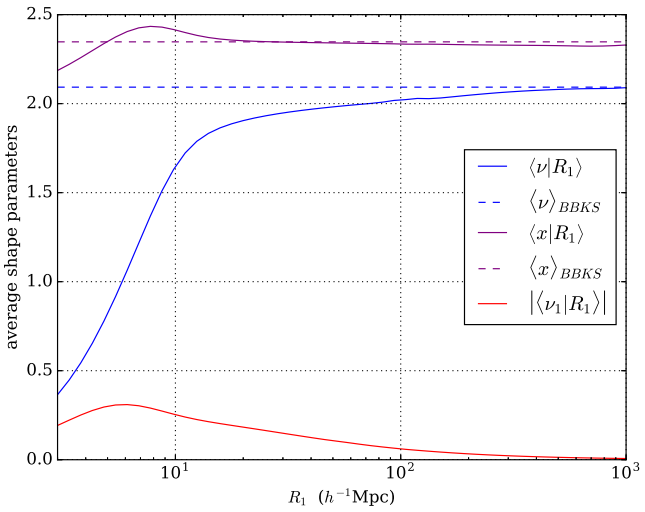

Figure 4. Mean expected values $\langle X|R_1\rangle$ for the shape parameters $X = \{\nu, x, \nu_1\}$ computed from equations (50), (53), and (55) as a function of the compensation radius. For illustration, the ΛCDM matter power spectrum has been smoothed on a Gaussian scale $R_f = 10\,h^{-1}$Mpc . The dashed lines are the expected values from BBKS with the condition equation (42) and are recovered for $R_1 \to \infty$ as shown in Section 3.2.3. Note that $\langle\nu_1|R_1\rangle \to 0$ in the $R_1 \to \infty$ limit.

marginalize the full joint probability distribution (see equation 35) over the central height ν and the curvature x

$$\frac{\mathrm{d}^2\mathcal{P}(\nu_1, R_1)}{\mathrm{d}\nu_1 \mathrm{d}R_1} = \int_{\nu_0}^{\infty}\int_0^{x_c} \frac{\mathrm{d}^4\mathcal{P}_{\rm tot}(\nu, x, \nu_1, R_1)}{\mathrm{d}\nu_1 \mathrm{d}R_1} \tag{46}$$

Note that ν is integrated from ν_0 to $+\infty$, where ν_0 is the lower threshold for the central height. The conditional probability $d\mathcal{P}(\nu_1|R_1)$ is deduced from Bayes theorem

$$\frac{\mathrm{d}\mathcal{P}(\nu_1|R_1)}{\mathrm{d}\nu_1} = \frac{\int_{\nu_0}^{\infty}\int_0^{x_c} \mathrm{d}^4 \frac{\mathcal{P}_{\rm tot}(\nu,x,\nu_1,R_1)}{\mathrm{d}\nu_1 \mathrm{d}R_1}}{\int_{\nu_0}^{+\infty} \mathcal{J}_{0,0}(\nu, R_1)\mathrm{d}\nu} \tag{47}$$

which describes the probability to get a compensated region with ν_1 given R_1 normalized such that $\int_{-\infty}^{0} \mathrm{d}\mathcal{P}(\nu_1|R_1) = 1$.

InFig. 3, we plot the distribution of δ_1 in a GRF with a comparison to numerical simulation, illustrating the excellent agreement between the theoretical expectation and the numerical results. As an illustration, if we neglect the dependence of x_c in term of ν_1 and the second term in equation (35), ν_1 follows a distribution of the form

$$\frac{\mathrm{d}\mathcal{P}(\nu_1|R_1)}{\mathrm{d}\nu_1} \propto |\nu_1| \exp\left[-\frac{(\nu_1 - \bar{\nu}_1)^2}{2\sigma^2}\right] \tag{48}$$

where $\bar{\nu}_1$ and σ are, respectively, the mean and dispersion value of the ν_1 distribution and are both functions of R_1.

From equation (47), we compute the moments of ν_1 given R_1, defined by

$$\left\langle \nu_1^n|R_1\right\rangle = \frac{\int_{\nu_0}^{+\infty} \mathcal{J}_{n,0}(\nu, R_1)\mathrm{d}\nu}{\int_{\nu_0}^{+\infty} \mathcal{J}_{0,0}(\nu)\mathrm{d}\nu} \tag{49}$$

where $\mathcal{J}_{n,m}$ generalizes the function defined in equation (45) as

$$\mathcal{J}_{n,m}(\nu, R_1) := \int_{-\infty}^{0} \nu_1^n \int_0^{x_c} x^m \frac{\mathrm{d}^4\mathcal{P}_{\rm tot}(\nu, x, \nu_1, R_1)}{\mathrm{d}\nu \mathrm{d}R_1}$$

For $n = 1$, we get the average value of ν_1 given R_1

$$\langle\nu_1|R_1\rangle = \frac{\int_{\nu_0}^{+\infty} \mathcal{J}_{1,0}(\nu, R_1)\mathrm{d}\nu}{\int_{\nu_0}^{+\infty} \mathcal{J}_{0,0}(\nu, R_1)\mathrm{d}\nu} \tag{50}$$

In Fig. 4, we plot $\langle\nu_1|R_1\rangle$ as a function of the compensation radius R_1 in a GRF (red curve). It admits a maximum for small compensation radius (here $R_1 \sim 10\ h^{-1}$Mpc as we used a Gaussian smoothing scale $R_f = 10\ h^{-1}$Mpc for the matter power spectrum) and slowly converges to 0.

3.3.3 *The height of the central peak ν*

The conditional probability distribution of the height ν of the central extremum given R_1 is obtained by integrating the full joint probability (see equation 35) over x and ν_1,

$$\frac{\mathrm{d}\mathcal{P}(\nu|R_1)}{\mathrm{d}\nu} = \frac{\mathcal{J}_{0,0}(\nu, R_1)}{\int_{\nu_0}^{+\infty} \mathcal{J}_{0,0}(\nu, R_1)\mathrm{d}\nu} \tag{51}$$

we deduce the moments of ν constrained by its cosmic environment i.e. for a given compensation radius

$$\langle\nu^n|R_1\rangle = \frac{\int_{\nu_0}^{+\infty} \nu^n \mathcal{J}_{0,0}(\nu, R_1)\mathrm{d}\nu}{\int_{\nu_0}^{+\infty} \mathcal{J}_{0,0}(\nu, R_1)\mathrm{d}\nu} \tag{52}$$

and in particular the average value for ν obtained for $n = 1$

$$\langle\nu|R_1\rangle = \frac{\int_{\nu_0}^{+\infty} \nu\mathcal{J}_{0,0}(\nu)\mathrm{d}\nu}{\int_{\nu_0}^{+\infty} \mathcal{J}_{0,0}(\nu)\mathrm{d}\nu} \tag{53}$$

As it can be seen in Fig. 4, $\langle\nu|R_1\rangle$ strongly depends on R_1 for small compensation radius while it progressively tends to its asymptotic value. As shown in Section 3.2.3, it converges to the standard value $\langle\nu\rangle$ computed by BBKS.

Small inhomogeneous regions (small R_1) are associated with lower central extremum, describing smoothed inhomogeneities, while higher extremum (or deeper voids) are more likely to sit in larger over massive (respectively, under massive) regions. As discussed in Section 3.2.3, the convergence towards the standard BBKS case illustrates the progressive decorrelation between the central peak and its large-scale cosmic environment.

3.3.4 The curvature distribution x

Finally, we evaluate the statistical properties of the local curvature x around a central extremum. Following the same development as before, we derive the various moments

$$\langle x^n|R_1\rangle = \frac{\int_{\nu_0}^{+\infty} \mathcal{J}_{0,n}(\nu, R_1)\mathrm{d}\nu}{\int_{\nu_0}^{+\infty} \mathcal{J}_{0,0}(\nu, R_1)\mathrm{d}\nu} \tag{54}$$

with the average of x given by

$$\langle x|R_1\rangle = \frac{\int_{\nu_0}^{+\infty} \mathcal{J}_{0,1}(\nu, R_1)\mathrm{d}\nu}{\int_{\nu_0}^{+\infty} \mathcal{J}_{0,0}(\nu, R_1)\mathrm{d}\nu} \tag{55}$$

We show in Fig. 4, the behaviour of $\langle x|R_1\rangle$ as a function of R_1. For large compensation radii, it converges to its modified BBKS value (see Section 3.2.3) and remains almost constant for a wide range of R_1. Again we observe on BAO scale some wiggles for $\langle \nu|R_1\rangle$ and $\langle x|R_1\rangle$ relating the peaks parameters and the compensation radius.

3.4 The mean average profile with a given compensation radius R_1 in GRF

3.4.1 The profile at fixed R_1

In the primordial Gaussian field, average profiles of CoSpheres are determined by four independent – but correlated – scalars; ν, x, ν_1, and R_1. At fixed compensation radius R_1, the other shape parameters $X = \{x, \nu, \nu_1\}$ can be considered as stochastic variables with constrained probabilistic distributions $\mathrm{d}\mathcal{P}(X|R_1)$ as computed in the previous sections. Since the average density and mass contrast profiles are linear in the shape parameters (see Paper I and equation 56), one can define the mean average profile at a fixed compensation radius as the profile whose shape parameters are averaged over their distribution, thus reaching

$$\frac{\overline{\langle\delta\rangle}(r)}{\sigma_0} = \langle\nu|R_1\rangle\,\delta_\nu(r) + \langle x|R_1\rangle\,\delta_x(r) + \langle\nu_1|R_1\rangle\,\delta_{\nu_1}(r) \tag{56}$$

where brackets mean an average on stochastic realization of the field and bar means an average over the possible values for the free shape parameters. The mass contrast profile reaches (Paper I)

$$\frac{\overline{\langle\Delta\rangle}(r)}{\sigma_0} = \langle\nu|R_1\rangle\,\Delta_\nu(r) + \langle x|R_1\rangle\,\Delta_x(r) + \langle\nu_1|R_1\rangle\,\Delta_{\nu_1}(r) \tag{57}$$

This profile describes the spherically compensated matter distribution resulting from stacking every possible realization at fixed R_1. In Fig. 5, we show the mass contrast profiles $\overline{\langle\Delta\rangle}$ for various compensation radii in ΛCDM cosmology. We retrieve the various properties of CoSpheres described before: (i) smaller central maxima (low ν) are associated with narrow compensation radius with a deep compensation density δ_1, (ii) higher central maxima (high ν) are located in larger over massive regions with a high R_1 and smoother density contrast δ_1 and (iii) when R_1 increases, central peaks become undistinguishable on small scales ($r \ll R_1$) and tend to the standard BBKS profiles. In other words, for large R_1, different environments with various compensation radii can be associated with very similar central profiles.

The whole of the previous discussion can be directly transposed to the symmetric case of a central minima, seeding cosmic void.

3.4.2 On the characteristic elbow

One particular feature of the mean average profile, besides the fact that they are fully determined by one single parameter R_1, is the existence of a characteristic elbow. This bend appears around $r \sim 10$ h^{-1}Mpc for profiles with $R_1 \geq 25$ h^{-1}Mpc (red curves in Fig. 5), but it also shows up in numerical profiles as can be seen in Fig. 1(b). This elbow is a result of the progressive decorrelation between the central peak and its surrounding environment as discussed in Section 3.2.3.

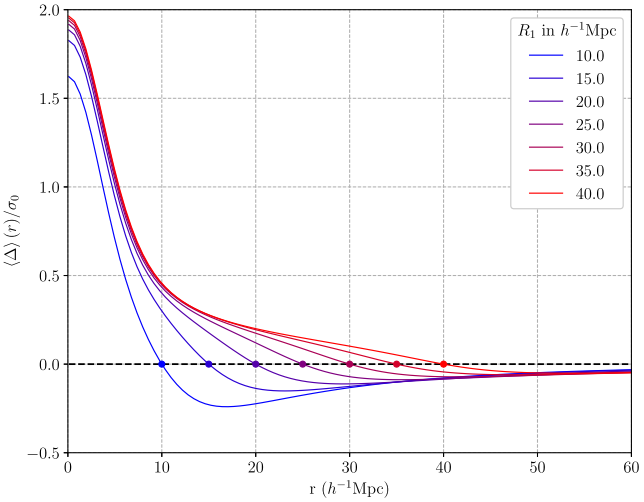

Figure 5. Mean average mass contrast profiles normalized to the fluctuation rms σ_0 for various compensation radius R_1 (from 10 to 40 h^{-1}Mpc) in a GRF (see equation 57). The elbow appearing beyond $r \sim 10$ h^{-1}Mpc for profiles with $R_1 > 30$ h^{-1}Mpc is not due to any dynamical feature, it is already present in the GRF and results from the compensation constraint. It illustrates that while the compensation radius R_1 increases, the central extrema is progressively isolated from its surrounding cosmic environment and its shape tends to the universal BBKS profile.

While R_1 increases, the central extremum tends to an universal shape as expected from BBKS. This elbow appears as the transition between small BBKS-like scales and larger ones involved with the compensation property. This characteristic does not appears in standard void profiles when build from their effective size $R_{\rm eff}$ as in Hamaus, Sutter & Wandelt (2014). This is likely due to the fact that voids with the same $R_{\rm eff}$ may have very different compensation radii. Stacking together profiles with the same $R_{\rm eff}$ may erase this feature. On the other hand, this elbow does not appears in evolved profiles build from central over densities as in Fig. 1(a) despite existing in the primordial Universe (see Fig. 5). This vanishing follows from the non-linear gravitational evolution of these profiles, altering their shape on small scales.

4 NON-LINEAR GRAVITATIONAL EVOLUTION OF COSPHERE IN ΛCDM COSMOLOGY

In the previous section, we discussed the statistical properties of the shape parameters of CoSpheres within the primordial GRF. These results stand under the Gaussian assumption which can be safely assumed at high redshift. In this section, we study the dynamical evolution of these quantities during the non-linear collapse of the matter field. As shown in Paper I, the adapted formalism for the gravitational collapse of these regions is the Lagrangian spherical collapse model (Padmanabhan 1993; Peacock 1998). It describes the Lagrangian evolution of concentric shells without shell-crossing or caustics formation.

4.1 Spherical Lagrangian collapse in ΛCDM cosmology

We recall the dynamical equations for the Lagrangian collapse suited for our study. In the following, a Greek letter χ will denote a *comoving* quantity, while a Latin character r designates a *physical* length. These quantities are related by $r = \chi \times a$ with a the homogeneous scale factor normalized as $a(t_0) = 1$ today. We also denote every initial quantity by the 'i' label, e.g. χ_i is the initial comoving position of one shell. Initial conditions are taken deep in the matter dominated era where the Gaussian assumption for $\delta(\boldsymbol{x})$ stands. We define the dimensionless Lagrangian displacement for each shell

$$\mathcal{R}(\chi_i, t) = \frac{\chi(t)}{\chi_i} \tag{58}$$

with $\chi(t)$ the comoving radius of the shell at some time t. The mass conservation in the absence of shell crossing leads to the relation

$$\frac{1+\Delta}{1+\Delta_i} = \mathcal{R}^{-3} \tag{59}$$

where Δ_i is the initial mass contrast for this shell, i.e. $\Delta_i = \Delta(\chi_i)$ and Δ its evolved mass contrast. In order to simplify the dynamical equation, we introduce the affine parameter τ defined through

$$\frac{\mathrm{d}\tau}{\mathrm{d}\log(a)} := \sqrt{\frac{\Omega_m}{2}} \tag{60}$$

which can be integrated to give $\tau(a)$ in the ΛCDM model, with the definition $\tau(a_i) = 0$

$$\tau(a) = \frac{\sqrt{2}}{3}\left[\mathrm{arctanh}\left(\Omega_{m,i}^{-1/2}\right) - \mathrm{arctanh}\left(\Omega_m^{-1/2}\right)\right] \tag{61}$$

With this new parametrization, the equation of motion driving the evolution of each individual shell reaches (Paper I)

$$\frac{\partial^2\mathcal{R}}{\partial\tau^2} + \frac{1}{\sqrt{2\Omega_m}}\frac{\partial\mathcal{R}}{\partial\tau} = \mathcal{R} - \frac{1+\Delta_i}{\mathcal{R}^2} \tag{62}$$

To close our system, we need to specify the initial conditions at $\tau = 0$. They are fixed by assuming that the dynamics follows the Zel'dovich evolution at very high redshift, leading to (Paper I)

$$\begin{cases} \mathcal{R}(t_i) & = 1 \\ \frac{\partial\mathcal{R}}{\partial\tau}(t_i) & = -\sqrt{\frac{2}{\Omega_{m,i}}}\frac{\Delta_i}{3} f(t_i) \end{cases} \tag{63}$$

where f is the linear growth rate (Peebles 1980) and $f(t_i)$ is evaluated at the initial time defined by $\tau = 0 \Leftrightarrow t = t_i$. Equation (62) is valid for any cosmology with a quintessence field sourcing DE and possibly a time-varying e.o.s. parameter w. The affine parameter τ is then still defined by equation (60), but equation (61) is no longer true (Alimi & de Fromont in preparation). We extend also equation (62) for theories beyond GRF in de Fromont & Alimi (in preparation).

4.2 Dynamical evolution of the compensation radius probability distribution

The particular scale R_1 is by definition conserved in comoving coordinates, i.e. $R_1(t) \propto a(t)$. In other terms, since the mean density enclosed in the sphere of radius R_1 equals the background density, this scale evolves as the scale factor of the Universe. Since R_1 is conserved, its probability distribution must also be conserved during the gravitational evolution. In principle, merging or creation of local extrema could modify this probability distribution. However, such effects are expected to occur on small scales, and since we consider sufficiently large value for R_1 ($R_1 \gtrsim 5$–$7\ h^{-1}$Mpc), the probability distribution $\mathrm{d}P(R_1)$ will not be affected.

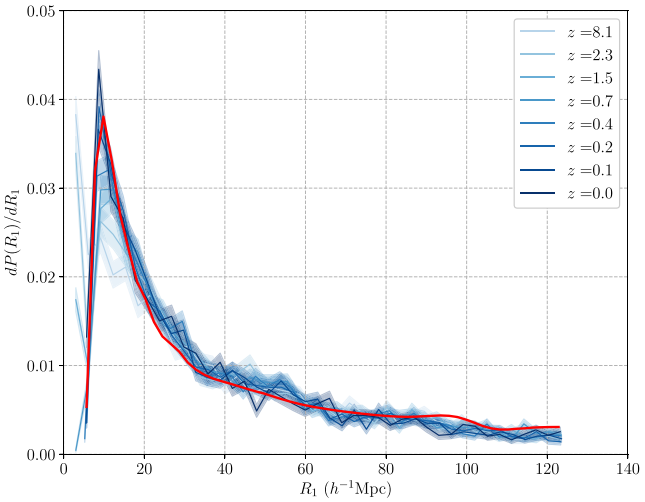

Figure 6. The compensation radius probability distribution $P(R_1)$ for ΛCDM cosmology computed from 10000 profiles build around haloes at various redshift ($z = 8$ to 0) in the reference simulation (blue lines). This figure has been obtained from 10 000 haloes of mass $M_h = 3.0 \pm 0.075 \times 10^{13}\ h^{-1}\,\mathrm{M}_\odot$. The shaded region around each curve is the Poisson noise computed in radial bins of size $\mathrm{d}R_1 = 3.5\ h^{-1}$Mpc. The red line is the initial Gaussian distribution given by equation (43). The conservation of R_1 ensures the conservation of its probability distribution. The height of the central threshold ν_0 has been chosen in agreement with the halo masses ($3.0 \times 10^{13}\ h^{-1}\,\mathrm{M}_\odot$) used to construct the compensated regions.

In Fig. 6, we show the measures of its probability distribution function (pdf) $\mathrm{d}P(R_1)/\mathrm{d}R_1$ at various redshifts from $z = 8$ to 0 in the numerical simulation. We also show the theoretical expectation from equation (43) computed within GRF. This figure illustrates two points. First, the compensation radius pdf does not evolve during the cosmic evolution excepted on very small scales ($R_1 \leq 5\ h^{-1}$Mpc) where our reconstruction procedure may be inaccurate (see Section 2). On larger scales however, neither the shape nor the amplitude are affected, confirming that this distribution is conserved during cosmic history.

On the other hand, the GRF expectation (see equation 43) fits the measured distribution with a very good agreement. This distribution thus appears as a good way to probe the early universe. However, since the initial power spectrum $P(k)$ is independent from the e.o.s. parameter for DE w, this probability distribution does not probe w neither σ_8, the amplitude of the power spectrum, but may probe Ω_m and the various quantities describing the primordial Universe as the scalar index n_s on very large scales. These cosmological dependencies are discussed in Alimi & de Fromont (in preparation).

Note however that the wiggles predicted by theoretical prediction around $R_1 \simeq 100\ h^{-1}$Mpc do not appears in numerical data. This may be due to the finite volume of our simulation ($L_{box} = 2592\ h^{-1}$Mpc) and the fact that on such scale, we are dominated by the cosmic variance (Rasera et al. 2014).

4.3 The evolution of the compensation density δ_1

δ_1 is defined on the sphere of radius R_1. It is a fundamental Eulerian quantity and its probability distribution can be computed analytically in the primordial GRF (see Section 3.3.2). δ_1 is directly measurable from the matter profile. In Paper I, we showed

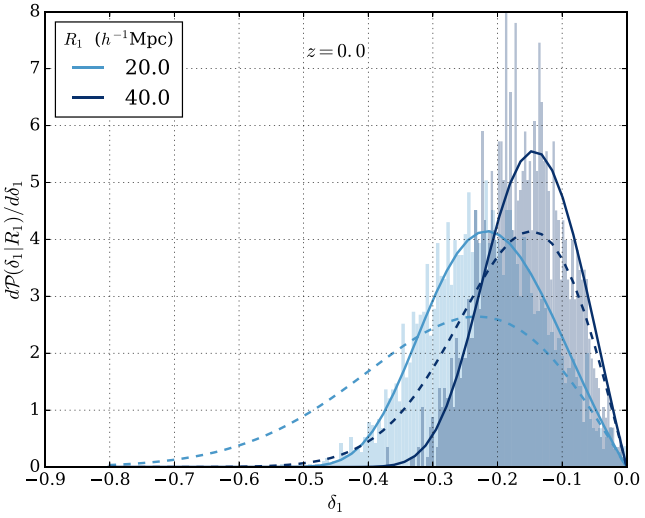

Figure 7. Evolved probability density function $\mathrm{d}P(\delta_1|R_1)/\mathrm{d}\delta_1$ at $z = 0$ in the ΛCDM cosmology from haloes. The full line curves correspond to the exact evolution given by equation (67). The shaded regions are the measured distributions for two different compensation radius in the reference simulation. The dashed curves are the Gaussian prediction, i.e. the linear evolution of the primordial distribution. This figure illustrates the non-linearity of the local gravitational process but also the possibility to reproduce the evolved distribution from the exact collapse.

that during the non-linear evolution, it follows a simple dynamics, corresponding to a one-dimensional Zel'dovich collapse

$$\delta_1^t = \delta_1 \frac{\tilde{D}(t)}{1 - \delta_1 \left(\tilde{D}(t) - 1\right)} \tag{64}$$

where $\tilde{D}(t)$ is the normalized linear growth factor defined by $\tilde{D}(t) = D(t)/D(t_\mathrm{i})$ and $\delta_1^t = \delta_1(t)$, while $\delta_1 = \delta_1(t_\mathrm{i})$ is its corresponding value in GRF. Equation (64) only holds at the particular point $r = R_1$ and cannot be extended to other arbitrary scale where Zel'dovich dynamics is, at best, an approximation. There is a bijective mapping between δ_1^t and δ_1 insuring that equation (64) can be inverted

$$\delta_1 = \frac{\delta_1^t}{\tilde{D}(t) + \delta_1^t \left(\tilde{D}(t) - 1\right)} \tag{65}$$

The computation of the non-linearly evolved conditional probability distribution $\mathrm{d}P(\delta_1^t|R_1)$ can be computed under the assumption that R_1 and the joint probability of δ_1 and R_1 are both conserved during evolution. Since δ_1 and δ_1^t are connected with a one-to-one relation, we have

$$\mathrm{d}P(\nu_1^t|R_1) = \mathrm{d}P(\nu_1|R_1) \tag{66}$$

with $\nu_1^t = \delta_1^t/\sigma_0$ and $\nu_1 = \delta_1/\sigma_0$, where σ_0 is computed in the primordial GRF only (and is a constant). Using equation (64), we get the conditional probability distribution at any time

$$\mathrm{d}P(\delta_1^t|R_1) = \frac{\tilde{D}(t)}{\left[\tilde{D}(t) + \delta_1^t(\tilde{D}(t) - 1)\right]^2} \left.\frac{\mathrm{d}P(\nu_1|R_1)}{\mathrm{d}\nu_1}\right|_{\nu_1 = \frac{\delta_1}{\sigma_0}} \frac{\mathrm{d}\delta_1^t}{\sigma_0} \tag{67}$$

where δ_1 and δ_1^t are linked by equation (65). In Fig. 7, we show the distribution $\mathrm{d}P(\delta_1^t|R_1)$ measured today in the reference simulation. Each curve corresponds to a compensation radius (here 20 and 40 h^{-1}Mpc). In each case, we show the non-linear prediction equation (67) in full line together with the linear evolution in dashed lines. The full spherical prediction reproduces the measured distribution with a high accuracy, whereas linear prediction predicts larger values of δ_1 today, especially for small compensation radii. It is interesting to note that the linear prediction also fails on large scales usually considered as 'linear', e.g. $R_1 = 40\,h^{-1}$Mpc . This difference come from the fact that despite being on 'linear' scales, this distribution probes high-density contrasts (δ_1 around -0.5) which are in the non-linear dynamical regime.

From equation (67), we can derive the average moments[3] of δ_1^t

$$\left\langle \delta_1^n | R_1 \right\rangle (t) = \int_{-1}^{0} \left(\delta_1^t\right)^n \mathrm{d}P(\delta_1^t|R_1) \tag{68}$$

where the integration is done over δ_1^t. Mapping δ_1^t to its corresponding value in the initial conditions δ_1 leads to

$$\left\langle \delta_1^n | R_1 \right\rangle (t) = \int_{-1}^{0} \left(\frac{\tilde{D}(t)\delta_1}{1 - \delta_1(\tilde{D}(t) - 1)}\right)^n \mathrm{d}P(\delta_1|R_1) \tag{69}$$

In Appendix B, we show that for both central minima and central maxima, these moments can be simply rewritten in term of the primordial moments in GRF

$$\left\langle \delta_1^n | R_1 \right\rangle (t) = \sum_{k \geq 0} \tilde{D}(t)^n \left(1 - \tilde{D}(t)\right)^k \binom{-n}{k} \left\langle \delta_1^{n+k} | R_1 \right\rangle \tag{70}$$

In particular, for $n = 1$, we get

$$\langle \delta_1 | R_1 \rangle (t) = \tilde{D}(t) \sum_{k \geq 0} \left(\tilde{D}(t) - 1\right)^k \left\langle \delta_1^{1+k} | R_1 \right\rangle \tag{71}$$

At $t = t_\mathrm{i}$, since $\tilde{D}(t_\mathrm{i}) = 1$, the only non-zero contribution comes from the $k = 1$ term leading to $\langle \delta_1 | R_1 \rangle$. Expanding equation (71), we have

$$\langle \delta_1 | R_1 \rangle (t) \simeq \tilde{D} \langle \delta_1 | R_1 \rangle + \tilde{D}(\tilde{D} - 1) \left\langle \delta_1^2 | R_1 \right\rangle + \cdots \tag{72}$$

The first term is the linear evolution, while higher terms account for the corrections to this simple dynamics. Note that equation (71) is different from the evolution of the mean which would be

$$\langle \delta_1 | R_1 \rangle (t) = \frac{\langle \delta_1 | R_1 \rangle \tilde{D}(t)}{1 - \langle \delta_1 | R_1 \rangle \left(\tilde{D}(t) - 1\right)} \tag{73}$$

whose small $\tilde{D}(t)$ expansion is

$$\langle \delta_1 | R_1 \rangle (t) \simeq \tilde{D} \langle \delta_1 | R_1 \rangle + \tilde{D}(\tilde{D} - 1) \langle \delta_1 | R_1 \rangle^2 + \cdots \tag{74}$$

The first linear term remains unchanged, while the second one differs by $\left\langle \delta_1^2 | R_1 \right\rangle - \langle \delta_1 | R_1 \rangle^2$. In Fig. 8, we show the measure of $\langle \delta_1 | R_1 \rangle (t)$ in the numerical simulations together with the exact evolution equation (71) and the various approximation equations (72) and (74) for $R_1 = 20\ h^{-1}$Mpc . We also show the linear prediction $\langle \delta_1 | R_1 \rangle = \tilde{D}(t) \langle \delta_1 | R_1 \rangle$. It turns out that the non-linear prediction fits very well the measured evolution on the whole range of reshifts.

The possibility to predict precisely the distribution of the compensation density at any non-linear redshift opens again new possibilities for cosmology and will be deeply studied in Alimi & de Fromont (in preparation) and de Fromont & Alimi (in preparation).

5 DISCUSSION AND CONCLUSION

In this paper, we derived the main statistical properties of CoSpheres as introduced in Paper I both in the primordial GRF and in the structured Universe until $z = 0$.

[3] Despite being a mute parameter, we prefer to keep the notation δ_1^t in the integral to highlight the fact that this average is evaluated at any time and not only in the initial conditions.

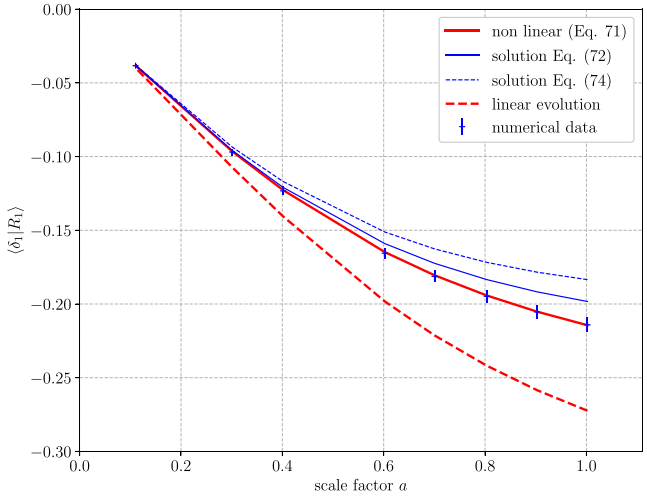

Figure 8. Redshift evolution of the first conditional moment of δ_1 at fixed R_1, $\langle\delta_1|R_1\rangle$ for $R_1 = 20\ h^{-1}$Mpc . Error bars are computed as the error on the mean estimated from 5000 single profiles. The red curve is the non-linear solution derived from Lagrangian spherical dynamics equation (71), the dashed red curve is the linear solution $\langle\delta_1|R_1\rangle(t) = D(t)/D(t_i)\langle\delta_1|R_1\rangle$ and the numerical data are in blue (points with corresponding error bars). The agreement between numerical and theoretical computations from equation (71) is very good for all redshift (here the x-axis is the scale factor $a = 1/(z+1)$. The full blue line and the dashed line are the small δ_1 expansion from equations (72) and (74). At low redshift, all the non-linear terms beyond the second-order term $\langle\delta_1|R_1\rangle$ have to be taken into account to reproduce the numerical results.

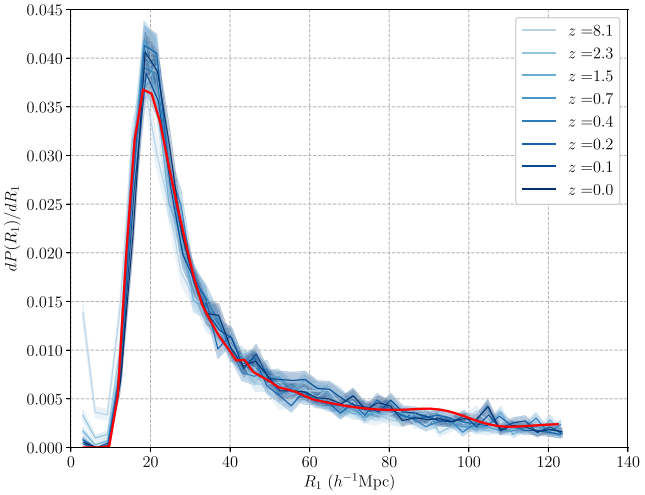

Figure 9. Probability distribution $\mathrm{d}P(R_1)/dR_1$ of the compensation radius R_1 from $z = 8$ to 0 centred on local minima. For this plot, the density field has been smoothed on a Gaussian scale $R_f = 5\ h^{-1}$Mpc . This figure has been obtained from 10 000 voids without selection criteria except that the central density contrast is negative. The shaded region around each curve is the Poisson noise computed in radial bins of size $\mathrm{d}R_1 = 3.5\ h^{-1}$Mpc . The red curve is the analytical prediction computed in the primordial Gaussian conditions equation (43), where the power spectrum has been smoothed on the equivalent Gaussian radius $R_g = 5\ h^{-1}$Mpc .

Within the Gaussian field, CoSpheres are fully determined by a unique compensation radius and a set of shape parameters ν, x, and ν_1. This formalism can be seen as a physical extension of the original BBKS work by taking explicitly into account the large-scale matter field around the local extremum. This extension describes the correlation between local extremum and their large-scale environment.

In the framework of GRF, we derive the full joint Gaussian probability for the four parameters R_1, ν, x, and ν_1 (see equation 35) by taking into account the appropriate domain for the curvature parameter x in order to ensure the correct definition of R_1 (see Section 3.2.2). Interestingly, as studied in Section 3.2.3, the very large-scale limit $R_1 \to +\infty$ reduces to the standard BBKS statistics for the central extrema BBKS. Physically, it describes the limit where the central extrema is completely decorrelated from its surrounding cosmic environment. In other words, the statistical distribution of ν or x are no more affected by R_1 when R_1 becomes very large.

Marginalizing the full joint probability over the shape parameters ν, x, and ν_1 leads to the distribution $\mathrm{d}P(R_1)$ (see equation 43) which gives the probability to find a CoSphere with a given R_1. Since each single R_1 is a comoving quantity, its pdf $\mathrm{d}P(R_1)$ is also expected to be conserved in comoving coordinates during the whole cosmic evolution. This is confirmed by Fig. 6, where we compare the R_1 distribution around DM haloes (central extremum) at various redshifts with the Gaussian prediction (red curve). Since the Gaussian field is exactly symmetric, this distribution can also be transposed without any change to the complementary case of central minimum, seeding cosmic voids. In Fig. 9, we show the compensation radius distribution $\mathrm{d}P(R_1)$ at various redshift for central minima. This figure has been obtained by finding minimum in the density field smoothed with a Gaussian kernel on $R_f = 5\ h^{-1}$Mpc at $z = 0$ and assuming that their position do not change with redshift (profiles are computed around the same position for each z). Once again, the Gaussian prediction (red curve) fits the measured distribution on all available scales.

As in Fig. 6, the BAO-like wiggles around $R_1 \sim 90\ h^{-1}$Mpc expected from theory do not appears clearly on numerical data. As previously discussed in Section 4.2, this slight discrepancy between theoretical and numerical results may be due to the cosmic variance which dominates on this scales due to the size of our simulation box (Rasera et al. 2014).

We emphasize that this distribution is suited to model the distribution of cosmic void sizes once identified as spherically compensated regions. This approach is fundamentally different from other attempts to model void statistics such as in Sheth & van de Weygaert (2004), Furlanetto & Piran (2006), and Achitouv et al. (2016). These approach are based on the excursion set theory (Press & Schechter 1974; Bond et al. 1991), while our formalism identifies the size of a void to its compensation radius. The improvement of our approach is the ability to define correctly the size of such cosmic structure and to be able to model its properties from first principles. However, our model assumes that we are indeed able to find this radius in observable data, which is far from being obvious.

Apart from the compensation radius distribution, we derived the statistical properties of the shape parameters of CoSpheres and particularly the conditional probability distribution of each shape parameter at fixed R_1. We computed their conditional moment and discussed the correlation between the central peak and its surrounding cosmic environment. More precisely, we have shown that whilst R_1 increases, the peak parameters ν and x progressively tend to their asymptotic BBKS value, while ν_1 vanishes. Small central extremum (small value of $|\nu|$) are associated with narrow compensation radii with a high compensation density ν_1. On the other hand, higher peaks are more likely to sit in large inhomogeneous regions with a small compensation density. Once again, this

discussion is valid for both central maximum and minimum, describing cosmic voids.

Using the spherical collapse model and the conservation of R_1, we then derived the evolved conditional distribution for δ_1 at fixed R_1. This leads to the evolved moments $\langle \delta_1^n | R_1 \rangle$ at $z = 0$ whose expression can be computed analytically. The comparison with numerical simulation are in a very good agreement with the Lagrangian prediction (see Figs 6 and 7). In the opposite, the Eulerian dynamical evolution fails to reproduce these quantities, even on 'large scales', e.g. $R_1 = 40\,h^{-1}\mathrm{Mpc}$.

The statistical properties of the compensation scalars R_1 and δ_1 are thus particularly interesting, since they can be directly measured in numerical simulations or otherwise from observational data and can be used as new cosmology probes. This is investigated in Alimi & de Fromont (in preparation) and de Fromont & Alimi (in preparation).

The fundamental interest of CoSpheres for cosmology is thus based on two main properties. The first one is the conservation of the compensation radius R_1 in comoving coordinates, i.e. the fact that that $R_1(t) \propto a(t)$. This fundamental feature implies the conservation of its probability distribution $\mathrm{d}P(R_1)$ during the whole cosmic history and allows in principle to probe directly the properties of the primordial Gaussian Universe. This property allows us to evaluate at $z = 0$ the statistics of the shape parameters describing both the small-scale extremum and its large-scale environment. The second fundamental property is the exact symmetric treatment of CoSpheres defined from central maximum or minimum. This formalism provides a physically motivated model for cosmic voids and offers an alternative approach for describing their statistical properties.

ACKNOWLEDGEMENTS

This work was granted access to HPC resources of TGCC and IDRIS through allocations made by GENCI (Grand Equipement National de Calcul Intensif) in the framework of the 'Grand Challenge' DEUS.

REFERENCES

Achitouv I., Neyrinck M., Paranjape A., 2015, MNRAS, 451, 3964
Achitouv I., Baldi M., Puchwein E., Weller J., 2016, Phys. Rev., D93, 103522
Alimi J.-M., Füzfa A., Boucher V., Rasera Y., Courtin J., Corasaniti P.-S., 2010, MNRAS, 401, 775
Alimi J.-M. et al., 2012, DEUS Full Observable LCDM Universe Simulation: the numerical challenge, IEEE Computer Society Press, CA, USA
Bardeen J. M., Bond J. R., Kaiser N., Szalay A. S., 1986, ApJ, 304, 15
Bertschinger E., 1987, ApJ, 323, L103
Bond J. R., Cole S., Efstathiou G., Kaiser N., 1991, ApJ, 379, 440
Cautun M., Cai Y.-C., Frenk C. S., 2016, MNRAS, 457, 2540
Courtin J., Rasera Y., Alimi J.-M., Corasaniti P.-S., Boucher V., Füzfa A., 2011, MNRAS, 410, 1911
de Fromont P., Alimi J.-M., 2018, MNRAS, 473, 5177
Furlanetto S. R., Piran T., 2006, MNRAS, 366, 467
Hamaus N., Sutter P. M., Wandelt B. D., 2014, Phys. Rev. Lett., 112, 251302
Jenkins A., Frenk C. S., White S. D. M., Colberg J. M., Cole S., Evrard A. E., Couchman H. M. P., Yoshida N., 2001, MNRAS, 321, 372
Komatsu E. et al., 2009, ApJS, 180, 330
Kowalski M. et al., 2008, ApJ, 686, 749
Neyrinck M. C., 2008, MNRAS, 386, 2101
Padmanabhan T., 1993, Structure Formation in the Universe. Cambridge Univ. Press, Cambridge
Peacock J. A., 1998, Cosmological Physics (Cambridge Astrophysics). Cambridge Univ. Press, Cambridge
Peebles P. J. E., 1980, Large-Scale Structure of the Universe. Princeton Univ. Press, Princeton, NJ
Platen E., Weygaert R. V. D., Jones B. J. T., 2007, MNRAS, 380, 551
Press W. H., Schechter P., 1974, ApJ, 187, 425
Rasera Y., Alimi J.-M., Courtin J., Roy F., Corasaniti P.-S., Füzfa A., Boucher V., 2010, in AIP Conf. Proc. Vol. 1241, Invisible Universe. Am. Inst. Phys., New York, p. 1134
Rasera Y., Corasaniti P.-S., Alimi J.-M., Bouillot V., Reverdy V., Balmés I., 2014, MNRAS, 440, 1420
Reverdy V. et al., 2015, Int. J. High Perform. Comput. Appl., 29, 249
Sheth R. K., Tormen G., 1999, MNRAS, 308, 119
Sheth R. K., van de Weygaert R., 2004, MNRAS, 350, 517
Tramonte D., no martin J. A. R., Betancort-rijo J., Vecchia C. D., 2017, MNRAS, 467, 3424
van de Weygaert R., Bertschinger E., 1996, MNRAS, 281, 84

APPENDIX A: COEFFICIENTS C_α

In this appendix, we give the explicit expressions of the C_α coefficients appearing in equation (24)

$$\frac{C_x}{\langle k^4 \rangle} = -\langle J_1 \rangle^2 \langle W_1^2 \rangle + 2\langle J_1 \rangle \langle W_1 \rangle \langle W_1 J_1 \rangle - \langle W_1 J_1 \rangle^2 + \langle J_1^2 \rangle \left[\langle W_1^2 \rangle - \langle W_1 \rangle^2 \right] \tag{A1}$$

$$C_\nu = -\langle J_1^2 \rangle \langle k^2 W_1 \rangle^2 - \langle k^4 \rangle \langle W_1 J_1 \rangle^2 + 2\langle k^2 J_1 \rangle \langle k^2 W_1 \rangle \langle W_1 J_1 \rangle + \langle W_1^2 \rangle \left[\langle J_1^2 \rangle \langle k^4 \rangle - \langle k^2 J_1 \rangle^2 \right] \tag{A2}$$

$$C_{\nu_1} = -\langle k^2 W_1 \rangle^2 + 2\langle k^2 \rangle \langle k^2 W_1 \rangle \langle W_1 \rangle - \langle k^2 \rangle^2 \langle W_1^2 \rangle + \langle k^4 \rangle \left[\langle W_1^2 \rangle - \langle W_1 \rangle^2 \right] \tag{A3}$$

$$\frac{C_{x\nu}}{\sqrt{\langle k^4 \rangle}} = \langle J_1^2 \rangle \langle k^2 W_1 \rangle \langle W_1 \rangle - \langle J_1^2 \rangle \langle k^2 \rangle \langle W_1^2 \rangle + \langle J_1 \rangle \langle k^2 J_1 \rangle \langle W_1^2 \rangle + \langle W_1 J_1 \rangle \left[\langle k^2 \rangle \langle W_1 J_1 \rangle - \langle J_1 \rangle \langle k^2 W_1 \rangle - \langle W_1 \rangle \langle k^2 J_1 \rangle \right] \tag{A4}$$

$$\frac{C_{x\nu_1}}{\sqrt{\langle k^4 \rangle}} = \langle k^2 J_1 \rangle \langle W_1 \rangle^2 - \langle J_1 \rangle \langle k^2 W_1 \rangle \langle W_1 \rangle + \langle W_1^2 \rangle \left[\langle J_1 \rangle \langle k^2 \rangle - \langle k^2 J_1 \rangle \right] + \langle W_1 J_1 \rangle \left[\langle k^2 W_1 \rangle - \langle W_1 \rangle \langle k^2 \rangle \right] \tag{A5}$$

$$C_{\nu_1 \nu} = \langle k^2 \rangle \langle k^2 J_1 \rangle \langle W_1^2 \rangle - \langle k^2 J_1 \rangle \langle k^2 W_1 \rangle \langle W_1 \rangle + \langle J_1 \rangle \left[\langle k^2 W_1 \rangle^2 - \langle k^4 \rangle \langle W_1^2 \rangle \right] + \langle W_1 J_1 \rangle \left[\langle k^4 \rangle \langle W_1 \rangle - \langle k^2 \rangle \langle k^2 W_1 \rangle \right] \tag{A6}$$

We also introduce C_0 defined by

$$C_0 = \left(\langle J_1 \rangle \langle k^2 W_1 \rangle - \langle k^2 J_1 \rangle \langle W_1 \rangle \right)^2 + \left(\langle k^2 \rangle^2 - \langle k^4 \rangle \right) \times \left(\langle J_1^2 \rangle \langle W_1^2 \rangle - \langle W_1 J_1 \rangle^2 \right) \tag{A7}$$

Linked to the determinant of the correlation sub-matrix $\tilde{\boldsymbol{Q}}$

$$\Sigma^2(R_1) = C_0 + C_{\rm x} + C_v + 2\frac{\langle k^2\rangle}{\sqrt{\langle k^4\rangle}}C_{{\rm x}v} \tag{A8}$$

Note that all these coefficients are functions of R_1.

APPENDIX B: COMPUTING THE EVOLVED MOMENTS OF THE COMPENSATION DENSITY

We now compute the evolved moments $\left\langle \delta_1^n|R_1\right\rangle(t)$ for both central minimum and maximum. We show that in both cases, it gives

$$\left\langle \delta_1^n|R_1\right\rangle(t) = \sum_{k\geq 0}\tilde{D}(t)^n\left(1-\tilde{D}(t)\right)^k\binom{-n}{k}\left\langle \delta_1^{n+k}|R_1\right\rangle \tag{B1}$$

where the various moments $\left\langle \delta_1^m|R_1\right\rangle$ are computed within the Gaussian field at some time $t_{\rm i}$ and $\tilde{D}(t) = D(t)/D(t_{\rm i})$.

B1 Central minima, i.e. cosmic voids

For central minimum seeding cosmic voids, the compensation density δ_1 is positive. Using the notations of Section 4.3, δ_1^t is the evolved compensation density and δ_1 its corresponding value in the primordial field. These quantities are linked through equations (64) and (65). Since we consider finite values of δ_1^t today, this implies that the corresponding primordial values must satisfy $\delta_1 \leq \delta_1^{\rm c}(t) \equiv 1/(\tilde{D}(t)-1)$ (see equation 64). The moments today are given by

$$\left\langle \delta_1^n|R_1\right\rangle(t) = \int_0^{+\infty}\left(\delta_1^t\right)^n {\rm d}P(\delta_1^t|R_1) \tag{B2}$$

Using the mapping equation (64), it leads to

$$\left\langle \delta_1^n|R_1\right\rangle(t) = \int_0^{\delta_1^{\rm c}(t)}\left(\frac{\tilde{D}(t)\delta_1}{1-\delta_1(\tilde{D}(t)-1)}\right)^n {\rm d}P(\delta_1|R_1) \tag{B3}$$

$$= \left(\sigma_0\tilde{D}(t)\right)^n\int_0^{1/\epsilon(t)}\left(\frac{\nu_1}{1-\nu_1\epsilon(t)}\right)^n {\rm d}P(\nu_1|R_1) \tag{B4}$$

where $\delta_1 = \sigma_0\nu_1$ and $\epsilon(t) = \sigma_0(\tilde{D}(t)-1)$. Since $\nu\in[0, 1/\epsilon(t)]$, we can use a Maclaurin expansion of the $1/(1-\nu_1\epsilon(t))$ term, leading to

$$\left\langle \delta_1^n|R_1\right\rangle(t) = \tilde{D}(t)^n\sum_{k\geq 0}(-1)^k\left(\tilde{D}(t)-1\right)^k\binom{-n}{k} \times\int_0^{1/\epsilon(t)}(\sigma_0\nu_1)^{n+k}\,{\rm d}P(\nu_1|R_1) \tag{B5}$$

Using the primordial moments $\left\langle \delta_1^n|R_1\right\rangle = \sigma_0^n\left\langle \nu_1^n|R_1\right\rangle$, we get the final result as recalled in equation (B1).

B2 Central maximum

For central maximum, the computation necessitates a careful treatment. We start from

$$\left\langle \delta_1^n|R_1\right\rangle(t) = \int_{-1}^0\left(\frac{\tilde{D}(t)\delta_1}{1-\delta_1(\tilde{D}(t)-1)}\right)^n {\rm d}P(\delta_1|R_1) \tag{B6}$$

Using equation (65), it is clear that if $\delta_1\geq -1$, then for any time t, we have $\delta_1^t\geq -1$. However, we cannot use here a Maclaurin expansion, since the term $\nu_1\epsilon(t) = \delta_1(\tilde{D}(t)-1))$ is no more included in its convergence radius, i.e. it can take values larger than 1 ($|\nu_1\epsilon(t)|>1$). We thus introduce the new variables $x = \delta_1+1$ and $\eta(t) = (\tilde{D}(t)-1)/\tilde{D}(t)$, both included in [0, 1]. Equation (B6) transforms to

$$\left\langle \delta_1^n|R_1\right\rangle(t) = \int_0^1\left(\frac{x-1}{1-x\eta(t)}\right)^n {\rm d}P(x-1|R_1) \tag{B7}$$

after a Taylor expansion in term of $\eta(t)$ and switching back to δ_1, we get

$$\left\langle \delta_1^n|R_1\right\rangle(t) = \sum_{k\geq 0}(-\eta(t))^k\binom{-n}{k}\left\langle \delta_1^n(1+\delta_1)^k|R_1\right\rangle \tag{B8}$$

Since $\delta_1\in[-1, 0]$, we expand also the term $(1+\delta_1)^k$ term,

$$\left\langle \delta_1^n|R_1\right\rangle(t) = \sum_{k\geq 0}(-\eta(t))^k\binom{-n}{k}\sum_{p=0}^k kp\left\langle \delta_1^{n+p}|R_1\right\rangle \tag{B9}$$

We simplify this expression by re-ordering and collecting terms with the same contribution,

$$\left\langle \delta_1^n|R_1\right\rangle(t) = \sum_{m\geq 0}\left[\sum_{k\geq m}(-\eta(t))^k\binom{-n}{k}\binom{k}{m}\right]\left\langle \delta_1^{m+n}|R_1\right\rangle \tag{B10}$$

Using again $\eta(t) = (\tilde{D}(t)-1)/\tilde{D}(t)$ together with the relation

$$\forall\alpha\in[-1, 1],\quad \sum_{k\geq m}\alpha^k\binom{-n}{k}\binom{k}{m} = \frac{\alpha^m}{(1+\alpha)^{m+n}}\binom{-n}{m} \tag{B11}$$

where $\alpha = (1-1/\tilde{D}(t)) = -\eta(t)$. We finally recover the same expression (B1), which holds for both central minima and central maxima.

This paper has been typeset from a TEX/LATEX file prepared by the author.